Hierarchical Composite Nanoarchitectonics with a Graphitic Core, Dendrimer and Fluorocarbon Domains, and a Poly(ethylene glycol) Shell as O 2 Reservoirs for Reactive Oxygen Species Production

Yitayal Admassu Workie, Cheng-Yu Kuo, Juwita Herlina Riskawati, Nattinee Krathumkhet, Toyoko Imae, Masaki Ujihara, Marie Pierre Krafft

Hierarchical composite nanoarchitectonics with a graphitic core, dendrimer and fluorocarbon domains, and a poly(ethylene glycol) shell as O_2 reservoirs for reactive oxygen species production

Yitayal Admassu Workie,[†] Cheng-Yu Kuo,[‡] Juwita Herlina Riskawati,[†] Nattinee Krathumkhet,[†] Toyoko Imae,[†,‡,ξ,*] Masaki Ujihara,[†] and Marie Pierre Krafft[§*]

[†]Graduate Institute of Applied Science and Technology, National Taiwan University of Science and Technology, Taipei 10607, Taiwan

[‡]Department of Chemical Engineering, National Taiwan University of Science and Technology, Taipei 10607, Taiwan

[ξ]Department of Materials Science and Engineering, National Taiwan University of Science and Technology, Taipei 10607, Taiwan

[§]University of Strasbourg, Institut Charles Sadron (CNRS), 67034 Strasbourg, France

Corresponding authors E-mail: imae@mail.ntust.edu.tw (T. I.), krafft@unistra.fr (M.P.K.)

ABSTRACT

Graphene oxide (GO), single-walled carbon nanohorn (CNHox), or nitrogen-doped CNH (N-CNH) were functionalized with fluorinated poly(ethylene glycol) (*F*-PEG) and/or with a fluorinated dendrimer (*F*-DEN) to prepare a series of assembled nanocomposites (GO/*F*-PEG, CNHox/*F*-PEG, N-CNH/*F*-PEG, N-CNH/*F*-DEN and N-CNH/*F*-DEN/*F*-PEG) that provide effective multisite O_2 reservoirs. In all cases, the O_2 uptake increased with time and saturated after 10-20 min. When graphitic carbons (GO and CNHox) were coated with *F*-PEG, the O_2 uptake doubled. The O_2 loading was slightly higher in N-CNH as compared to CNHox. Notably, coating N-CNH with *F*-DEN or *F*-PEG, or with both *F*-DEN and *F*-PEG, was more effective. The best performance was obtained with the N-CNH/*F*-DEN/*F*-PEG nanocomposite. The O_2 uptake kinetics and mechanisms were analyzed in terms of Langmuir adsorption equation based on a multi-binding site assumption. This allowed the precise determination of multiple oxygen binding sites, including on the graphitic structure and in the dendrimer, *F*-DEN and *F*-PEG. After an initial rapid, relatively limited release, the amount of O_2 trapped in the nanomaterials remained high (> 95%) amount. This amount was marginally lower for the functionalized composites, but the oxygen stored was reserved for longer

times. Finally, it is shown that these systems can generate singlet oxygen after irradiation by a light-emitting diode, and this production correlates with the amount of O_2 loaded. Thus, It was anticipated that the present nanocomposites hierarchically assembled from components with different characters and complementary affinities for oxygen can be useful as O_2 reservoirs for singlet oxygen generation to kill bacteria and viruses and to perform photodynamic therapy.

Key Words: Oxygen carrier; Graphene oxide; Single-walled carbon nanohorn; Fluorinated poly(ethylene glycol); Fluorinated dendrimer; Hierarchical nanocomposite; Reactive oxygen species, Photodynamic therapy; Gas reservoir

INTRODUCTION

Oxygen has a vital role in maintaining the normal physiological function of the human body. It plays a crucial role in the cellular microenvironment that controls the cell viability and differentiation, the adenosine triphosphate (ATP) production, and the regulation of metabolic processes. Hypoxia, which is characterized by an insufficient level of oxygen in the tissues, can induce apoptosis and necrosis of the cells. Hypoxia is related to numerous pathologies from inflammation to cancer.[1-3] O_2 carriers are an alternative to blood for improving tissue and organ oxygenation.[4-12] However, although several biomaterials were reported to deliver oxygen, there still are limitations like vasoconstriction in the case of hemoglobin-based products and other side effects or intolerance by patients, and hence the search for safer and more effective O_2 carriers is nessary.[6,7] Oxygen delivery can be achieved using perfluorocarbon emulsions,[4-6,8,10,13] synthetic hemes and hemoglobin-based carriers.[6-8] The O_2 carrier properties of perfluorocarbon emulsions are due to the unique gas dissolving properties of perfluorocarbons combined to their chemical inertness.[4-6,10,12,14] Perfluorocarbons exhibit low intramolecular cohesion and can provide a suitable microenvironment for O_2 molecule storage in a liquid phase. The affinity of oxygen to solid matrices,[12] including graphene oxide[15] has also been investigated to design effective O_2 carriers. The use of fluorinated zeolites to store and transport O_2 was suggested too.[16] Designing such a perfluorocarbon-rich microenvironment could improve the efficiency of oxygen loading in graphitic nanomaterials, and this is the challenge addressed in this article.

Like graphene oxide (GO), oxidized single-walled carbon nanohorn (CNHox) is a new class of carbon-based nanomaterials that is attracting attention as promising materials.[17,18] Carbon

nanohorn (CNH) is a graphitic material consisting of nanometer-sized horns with unique applicability in biosensor technology,[19] bioimaging,[20] photodynamic therapy,[21] drug delivery[22,23] and gas storage.[24,25] CNH can be functionalized by carboxylation, oxidation or nitridization and can be hybridized with different polymeric materials to enhance biocompatibility and water dispersibility. Introduction of heteroatoms (oxygen or nitrogen) helps adjusting the chemical properties of CNHox for controlling its reactivity. Typical polymers used for hybridization are poly(ethylene glycol),[26] sugar-based derivatives,[27] and poly(amido amine) (PAMAM) dendrimers.[28] PAMAM dendrimers have a regularly branched three-dimensional spherical morphology with many voids that can host small molecules, and abundant terminal functional groups that can help controlling the affinity for various materials. These dendrimers thus offer a great versatility, a high selectivity and a definite potential for gas storage.[29,30] Hybridized composites with oxygen-doping ability could be applied to oxygen delivery, although this use has not yet been reported to our knowledge.

Hierarchical composites composed of CNHox, PAMAM dendrimers grafted with pentafluoropropionic acid (*F*-DEN) and fluorinated poly(ethylene glycol) (*F*-PEG) were shown to load nitric oxide efficiently.[26,31] Related materials based on acid-treated nitrogen-doped CNH (N-CNH) are also expected to exhibit oxygen carrying capacity through functionalization by *F*-DEN and *F*-PEG, as demonstrated for nitric oxide.[26,31] In this work, the graphitic materials GO, CNHox and N-CNH were hierarchically functionalized with *F*-DEN and *F*-PEG to form various composites of GO/*F*-PEG, CNHox/*F*-PEG, N-CNH/*F*-PEG, N-CNH/*F*-DEN and N-CNH/*F*-DEN/*F*-PEG, with the expectation that the assembled systems efficiently increase O_2 uptake and function as novel biocompatible gas reservoir systems. The O_2 uptake was measured for the various composites synthesized, and their efficiency was compared. The O_2 uptake profiles were analyzed based on the Langmuir adsorption kinetics theory, which allowed determination of binding site species and oxygen amount on each site. The O_2 releasing profiles are determined by a thermogravimetric analysis at 37 °C. Finally, the capacity of composites to generate singlet oxygen was measured by fluorescence spectroscopy.

EXPERIMENTAL

Materials and Methods

Oxidized single-walled carbon nanohorn CNH_{ox} was provided by NEC Corporation, Japan. Ethyl carbodiimide (EDC), N-hydroxysuccinimide (NHS), N,N'-dicyclohexylcarbodiimide (DCC, 99%), 4-dimethylaminopyridine (DMAP, 99%), and N,N-dimethylformamide (DMF, >99%) were from ACROS organics, Belgium. Pentafluoropropionic acid (97%) was purchased from Fluorochem, UK. Hydroxyl- and amine-terminated PAMAM dendrimers (DEN(OH) and $DEN(NH_2)$, ethylenediamine core, generation 4.0, 10 wt% in methanol) were from Sigma-Aldrich, USA. GO, *F*-PEG, *F*-DEN, and the composites GO/*F*-PEG, N-CNH, N-CNH/*F*-DEN, and N-CNH/*F*-DEN/*F*-PEG were the same materials that have been synthesized and characterized in the previous reports.[26,31] Other chemicals were of commercial grade, and all reagents were used without further purification. Ultrapure water (resistivity of 18.2·MΩ cm, Yamato Millipore WT100, Japan) was used throughout this study.

The characterization of the materials was performed by transmission electron microscopy (TEM, JEOL-2000 FX II, Japan, 120 kV), scanning electron microscopy (SEM, JSM-6390, Japan, 15 kV) equipped with an energy-dispersive X-ray spectroscopy (EDS) analyzer, atomic force microscopy (AFM, NanoScope III, Veeco Digital Instrument, USA, contact mode), dynamic light scattering (DLS, SZ-100, HORIBA scientific and ELSZ-1000 series, OTSUKA, Japan), X-ray diffractometry (XRD, D2 Phaser, Bruker, USA), Fourier transform infrared (FT-IR) absorption spectrometry (Nicolet 6700, Thermo Scientific, USA), ultraviolet (UV)–visible absorption spectrometry (JASCO V-670, Japan), fluorescence spectrometry (Hitachi-7000, Japan), thermogravimetry (TGA, TA Q500, USA), Raman scattering (Horiba Jobin Yvon iHR550, Japan) and X-ray photoelectron spectrometry (XPS, VG Scientific, ESCALAB 250, UK).

Preparation of nanocomposites

GO grafted with the fluorinated dendrimer *F*-DEN(OH) (GO/*F*-DEN) was synthesized by an esterification reaction in DMF as shown in **Supporting Information Figure S1A**. A pentafluoropropionic acid solution (10 mM in DMF, 140 µl) was sonicated for 10 min with excess DCC (10 mM in DMF, 150 µl) and DMAP (10 mM in DMF, 30 µl). To this solution, a DEN(OH) solution (0.2 wt% in DMF, 10 ml) was added at a DEN(OH):pentafluoropropionic acid molar ratio of 1:1, and stirred for 1 day at room temperature. Subsequently, after GO (1.2 mg in DMF, 4 ml) was mixed with excess DCC/DMAP, *F*-DEN(OH) in DMF (4 ml) was added and stirred for 1 day at room temperature. The product was washed with DMF and water.

The synthesis of *F*-DEN(NH_2), achieved with a NH_2:pentafluoropropionic acid molar ratio of 1:1.6, was performed based on an amidation reaction in water. After methanol in a DEN(NH_2) solution (10 wt%, 1.02 g) was evaporated, water (50.9 g) was added to make a DEN(NH_2) solution (0.2 wt%). After an aqueous pentafluoropropionic acid solution (10 mM, 140 μl) was stirred for 1 h with an excess EDC (10 mM in water, 150 μl) and NHS (10 mM in water, 150 μl), an aqueous DEN(NH_2) solution (0.2 wt%, 8 ml) was added and stirred at room temperature for 1 day. Successively, an aqueous GO suspension (0.3 mg/ml, 2 ml) was mixed with EDC and NHS, and after stirring for 1 h, an aqueous *F*-DEN(NH_2) solution (2 ml) was added. Then the mixed suspension was kept under stirring at room temperature for 1 day, and the residue (GO/*F*-DEN(NH_2)) obtained after centrifugation was rinsed three times with water. GO/*F*-DEN (0.3 mg/ml, 1 ml) was mixed with *F*-PEG (in water, 1 ml) at various concentrations and sonicated for 10 min.

The CNHox/*F*-PEG composite was prepared by dispersing CNHox (12 mg) in water (40 ml) and sonicating the dispersion for 30 min in a bath sonicator. Equal volumes of CNHox (300 μg/ml) and *F*-PEG (24 μg/ml) dispersed in water were mixed and stirred for 24 h. Similarly, N-CNH/*F*-DEN (300 μg/ml) and *F*-PEG (24 μg/ml) in water were mixed and stirred for 24 h. The resulting dispersion was filtered on a cellulose acetate membrane (200 nm-sized pores), and the residual slurry was dried at room temperature.

Uptake and release of O_2

Efficiencies of composites (GO, GO/*F*-PEG, CNHox, CNHox/*F*-PEG, N-CNH, N-CNH/*F*-DEN and N-CNH/*F*-DEN/*F*-PEG) in uptaking and releasing O_2 were measured by exposing the materials to air in a closed system. The material (10 mg) was vacuumed for 3 h at 100 °C to remove the adsorbed molecules and gases. Immediately after the degassing process, the initial weight of the material was accurately measured by TGA, and air from a cylinder was then filled in the closed system for 8 h at room temperature under atmospheric pressure. The weight gain of the material was measured during and after O_2 loading. The release profiles of O_2 from the materials (GO, GO/*F*-PEG, CNHox, and CNHox/*F*-PEG) were examined using TGA after the desorption for 400 min at body temperature (37 °C).

Detection of singlet oxygen generation

After the saturation with O_2 for 60 min, the composites were utilized to measure singlet oxygen generated by an LED irradiation (450 nm, 0.08 Wcm^{-2}). This was achieved using an anthracene probe that is oxidized by singlet oxygen.[32] Anthracene in methanol (20 µg/ml, 1 ml) was mixed with the test composites at a concentration of 2.5 µg/ml. The fluorescence spectra of the mixtures at an excitation wavelength (320 nm) of anthracene were recorded before and after 10 min irradiation with the LED lamp. The emission area intensities were integrated, and the generated singlet oxygen was calculated using the following equation:

$$Singlet\ oxygen\ generation = \frac{(I_0 - I_t)}{grad} \cdot \frac{V}{MW_{Standard}} \qquad (1)$$

where $MW_{standard}$ is the molecular weight of anthracene (178.23 g/mole), I_0 and I_t are the emission area intensities before and after radiation for 10 min, grad is the gradient of the calibration curve (ml/mg) and V is the total volume of the test solution (1.5 ml).

RESULTS AND DISCUSSION

Characteristics of GO/*F*-DEN and GO/*F*-DEN/*F*-PEG composites

The GO/*F*-DEN composite with an OH- terminated PAMAM dendrimer was well dispersed in water (**Figure S1B**), by contrast to the composite with NH_2-terminated PAMAM dendrimer that showed poor dispersibility in aqueous media, aggregated and precipitated after 30 min. **Figure S1C** shows the IR absorption spectra of the materials. The spectrum of GO exhibited an absorption band at 1705 cm^{-1} associated to a C=O (COOH) stretching mode, which was obviously diminished after esterification with *F*-DEN, indicating that GO and *F*-DEN were chemically bound. Furthermore, GO/*F*-DEN showed absorption bands of amide I and amide II vibration modes of DEN(OH) at 1638 cm^{-1} and 1548 cm^{-1}, respectively. Similar variations of IR bands were also seen for GO/Den(OH). The characteristic bands of C-F, originating from pentafluoropropionic acid around 1200-1250 cm^{-1} appeared on GO/*F*-DEN, but not on GO/DEN(OH). EDS analysis on SEM showed the existence of nitrogen and fluorine elements besides carbon and oxygen in GO/*F*-DEN (**Figure S1(D)**). This result also indicates that *F*-DEN was successfully bound on GO.

TEM images revealed the flat single sheet shape of GO/*F*-DEN(OH), similar to GO (**Figure 1Aa, b**). In addition, AFM images also showed flat sheets for GO and GO/*F*-DEN (**Figure 1Ba, b**), in agreement with TEM images, but their section analyses indicated a difference in height

between the two materials (**Figure 1Ca, b**): The height of GO/*F*-DEN sheets (5.34 ± 1.00 nm) was higher than for GO (1.84 ± 0.10 nm). This difference might be due to the immobilization of *F*-DEN on both sides of the GO sheet. The thickness of GO sheets is comparable to that of graphene sheets, as estimated by AFM.[33] In this stratified structure, the thickness of the dendrimer layers can thus be evaluated to be 1.75 nm ± 0.55 nm (see **Figure 1Da,b**). This value is comparable to the thickness of a dendrimer lying flat on a surface.[34]

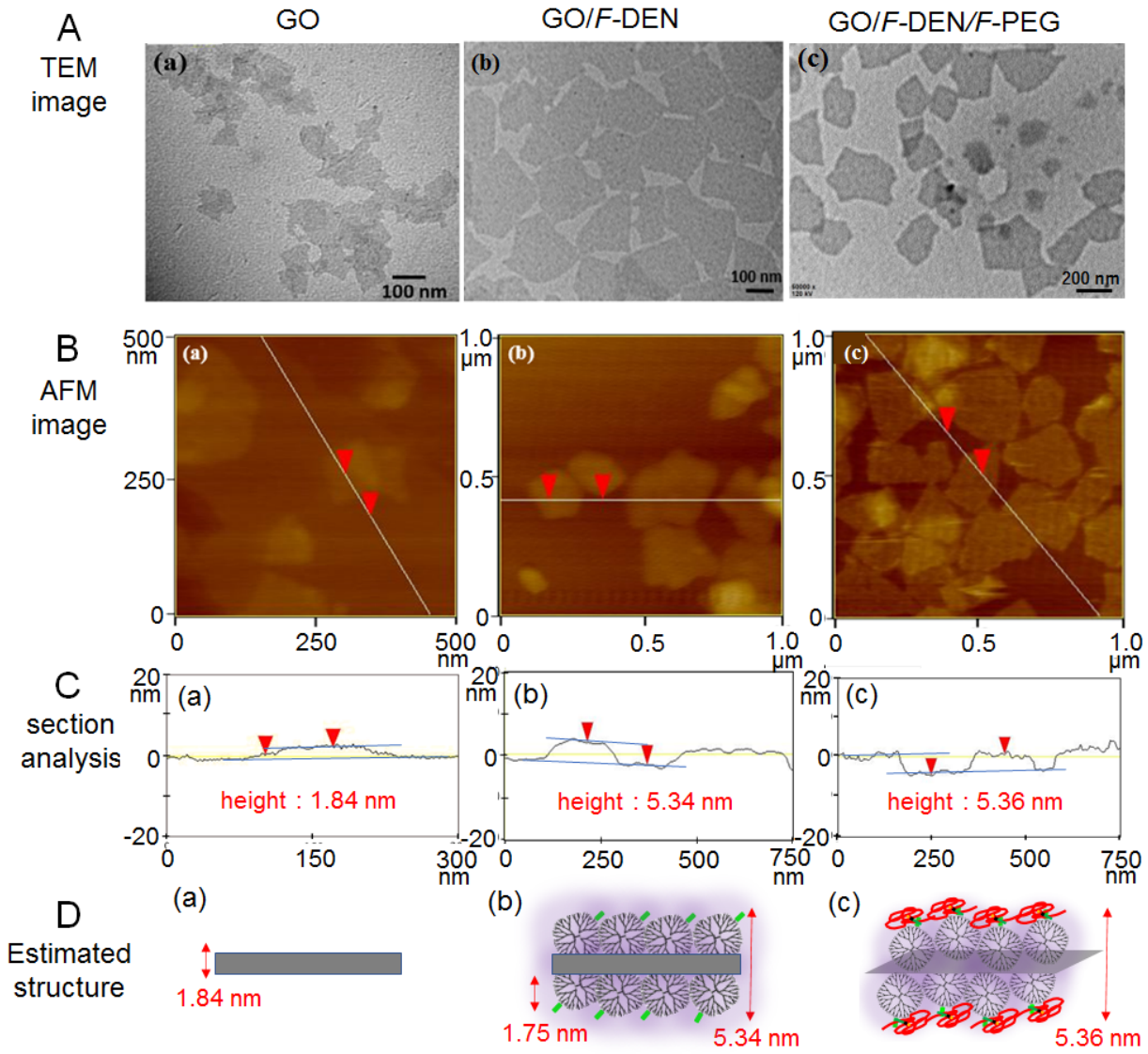

Figure 1 (A) TEM images, (B) AFM images, (C) section analyses of AFM images and (D) proposed structures of (a) GO, (b) GO/*F*-DEN and (c) GO/*F*-DEN/*F*-PEG. The blue lines in Figure C are indicator lines for height measurements.

When the pH of aqueous GO/*F*-DEN dispersions was changed from the initial value (6-7) to acidic and alkaline conditions, the average hydrodynamic particle size measured by DLS was around 362 ± 22 nm, being almost independent of pH (**Figure S2A)**. As the hydrodynamic diameter of GO was 119 nm, in agreement with previous reports,[18,31] the increase in size of GO/*F*-DEN indicates successful immobilization of *F*-DEN on GO.

The zeta potential of GO/*F*-DEN depended remarkably on the pH of the solution, although the zeta potential of GO was always negative in the whole range of pH examined (data not shown): According to results in **Figure S2B**, net positive charges were obtained in acidic conditions (pH 2 to 5) with the highest zeta potential value at pH 3-4, and negative charges were obtained for pH 6 to 13, the highest value being measured at pH 9-10. These charges resulted from the protonated tertiary amine of the PAMAM dendrimer and the deprotonated carboxylic acid on GO, respectively. Then the zeta potential approached zero at pH 5-6, which corresponds to the isoelectric point. Thus, GO/*F*-DEN(OH) was stably dispersed in the whole pH region, except for pH 4-6. Incidentally, although the composite GO/*F*-DEN**(**NH_2**)** also displayed an isoelectric point at pH 5-6, the positive zeta potentials at pH 2-5 were always lower than 20 mV, supporting a lesser dispersibility for GO/*F*-DEN(NH_2) than for GO/*F*-DEN(OH) (**Figure S2D**). For this reason, only *F*-DEN(OH) is used in the following, and its notation simplified to *F*-DEN.

The morphology of GO/*F*-DEN/*F*-PEG was also observed by TEM and AFM, as shown in **Figure 1Ac** and **1Bc**, respectively. Both images indicated plate-like morphologies, which were similar to those obtained for GO/*F*-DEN. Meanwhile, the average height of GO/*F*-DEN/*F*-PEG sheets from the AFM section analysis was 5.36 ± 1.00 nm (see **Figure 1Cc**), which was comparable to that of GO/*F*-DEN (5.34 nm). To assess the difference between GO/*F*-DEN and GO/*F*-DEN/*F*-PEG, the surface analyses of AFM images were compared, as shown in **Figure 2**. The roughnesses of GO/*F*-DEN and GO/*F*-DEN/*F*-PEG were 1-1.5 nm and 2-3 nm, respectively, although the shape and height of plates formed by two composites were almost similar. This result points out the adsorption of *F*-PEG on the surface of GO/*F*-DEN, driven by the interaction between *F*-DEN and *F*-PEG. That is, the adsorption of *F*-PEG on the GO/*F*-DEN surface significantly impacted the roughness of the material in the dry state (see **Figure 1Dc**).

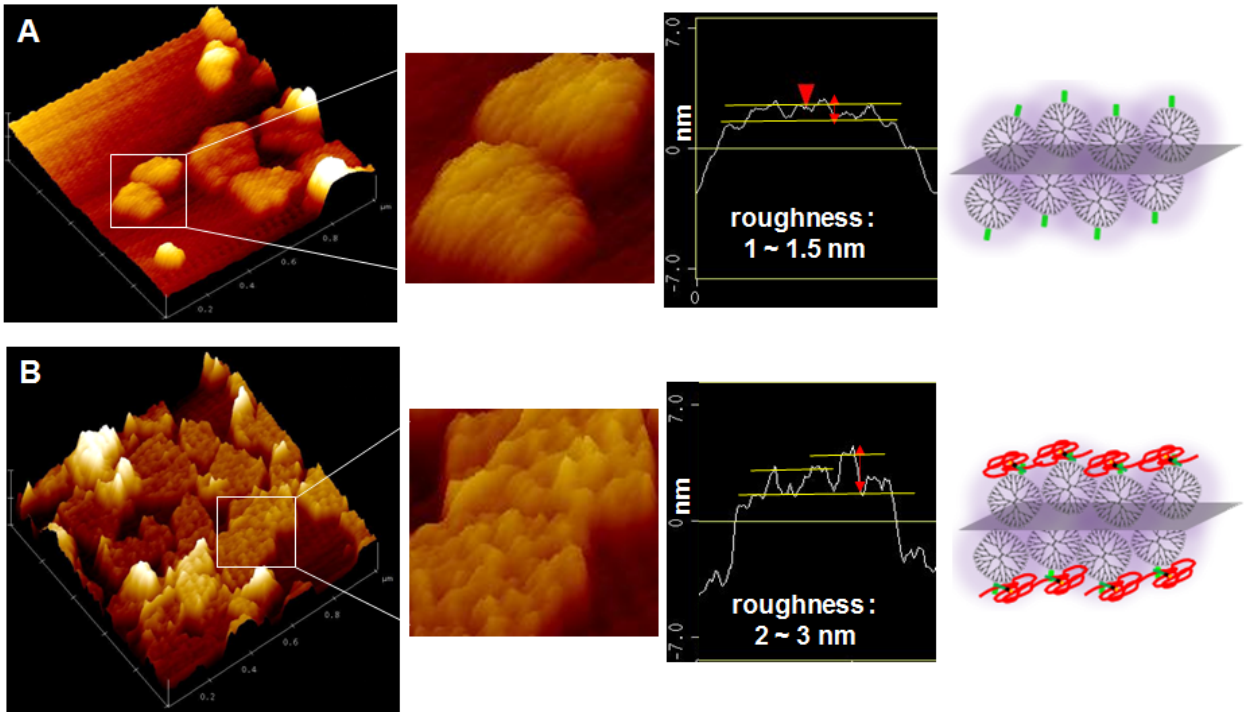

Figure 2 The 3D AFM images (in 1x1 μm^2 size), magnified images, cross-section analyses, and proposed models of (A) GO/*F*-DEN and (B) GO/*F*-DEN/*F*-PEG. The yellow lines in cross-section analyses are indicator lines for height measurements.

Aqueous dispersions of GO/*F*-DEN/*F*-PEG were adjusted at different pH and measured by DLS; their zeta potentials were also acquired. According to **Figure S2A**, the hydrodynamic mean size of GO/*F*-DEN/*F*-PEG was 300-400 nm in the whole pH region from 2 to 12. The fact that only a single peak was obtained in the DLS measurement confirmed that *F*-PEG was adsorbed on GO/*F*-DEN (**Figure S2C**). The mean size was about 50 to 100 nm larger than that of GO/*F*-DEN, and this increase may be attributed to the swelling of *F*-PEG on GO/*F*-DEN in water. Incidentally, the lesser increase in the height of GO/*F*-DEN/*F*-PEG compared to GO/*F*-DEN, as measured by AFM, can be interpreted by lesser or no swelling of *F*-PEG on GO/*F*-DEN in dry conditions.

As *F*-PEG contains a PEG chain, a short alkyl chain and a fluoroalkyl chain, this amphiphilic molecule can form self-assemblies when dispersed in water. The DLS measurement of *F*-PEG aqueous dispersions revealed a bimodal distribution centered on 80-180 nm and 1200-2200 nm at a concentration range of 5-220 nM (see **Figure S2E**), suggesting the coexistence of monomers and aggregates of *F*-PEG. However, the DLS profiles of aqueous GO/*F*-PEG dispersions displayed only a single peak at around 200-300 nm for various concentrations of composites. This indicates

that *F*-PEG is preferentially adsorbed on the GO surface rather than forming self-assemblies, and that GO/*F*-PEG constitutes a stable arrangement in aqueous media as illustrated in **Figure S2F**. The perfluorinated moiety of *F*-PEG may adsorb close to the graphitic domains of GO in GO/*F*-PEG, since both are hydrophobic, but the adsorption of *F*-PEG occurred through hydrophobic/oleophobic interactions with the perfluorinated moiety of *F*-DEN in the case of GO/*F*-DEN/*F*-PEG (**Figure S2C**).

The zeta potential of GO/*F*-DEN/*F*-PEG exhibited positive charges at pH 2-6, and negative charges at pH 6-13 (see **Figure S2B**). Moreover, the values of zeta potential were quite high (with an absolute value higher than 30 mV) at most pH except for pH 5.5 ~ 6, which corresponds to the isoelectric point. Thus, it can be concluded that the GO/*F*-DEN/*F*-PEG composite exhibits high stability in aqueous media at most pH values. These behaviors were almost similar to those of GO/*F*-DEN, because the electrokinetic phenomenon mainly occurred from the charged GO and DEN but was not influenced by nonionic *F*-PEG, although the isoelectric point was slightly shifted to higher pH and the zeta potential was shifted to negative values after the adsorption of *F*-PEG.

Characterization of CNHox/*F*-PEG Composites

The morphologies and particle size distributions of CNHox and CNHox/*F*-PEG composites were investigated using TEM and DLS. As presented in **Figure 3A**, CNH appeared as spheroidal particles with diameters lower than 100 nm,[26] and the CNHox/*F*-PEG composite presented a comparable spherical structure. However, while CNHox presented a hydrodynamic mean size of 138 nm, the adsorption of *F*-PEG on CNHox caused a significant increase in the mean size (200 nm). The size variation of the composite from pristine CNHox indicates that *F*-PEG is bound on CNHox by favored hydrophobic/oleophobic interactions, as observed for GO/*F*-PEG. The result excludes the coexistence of isolated *F*-PEG aggregates and CNHox.[31]

The presence of *F*-PEG in the CNHox/*F*-PEG material was assessed by an FT-IR absorption spectroscopy as presented in **Figure 3B**. The FT-IR absorption bands of *F*-PEG are ascribed to O-H (H_2O) stretching (3430 cm^{-1}), alkane CH_2 stretching (2910 cm^{-1}), O-H (H_2O) bending (1640 cm^{-1}), CH_2 scissoring (1460 cm^{-1}), CH_2 wagging (1350 cm^{-1}), CH_2 twisting (1258 cm^{-1}), C-F stretching (1110 cm^{-1}) and C–O–C stretching (949 cm^{-1}) vibration modes.[31] An FT-IR spectrum of CNHox showed O-H stretching (3440 cm^{-1}), CH_2 antisymmetric and symmetric stretching (2920 cm^{-1} and 2860 cm^{-1}, respectively), C=O stretching (1730 cm^{-1}), C=C stretching (1590 cm^{-1}),

C-C stretching (1380 cm^{-1}), and C-O-C stretching (1120 cm^{-1}) bands.[26] The spectrum of CNHox/*F*-PEG composite exhibited all the FT-IR bands of each component, confirming the coexistence of both components in the material.

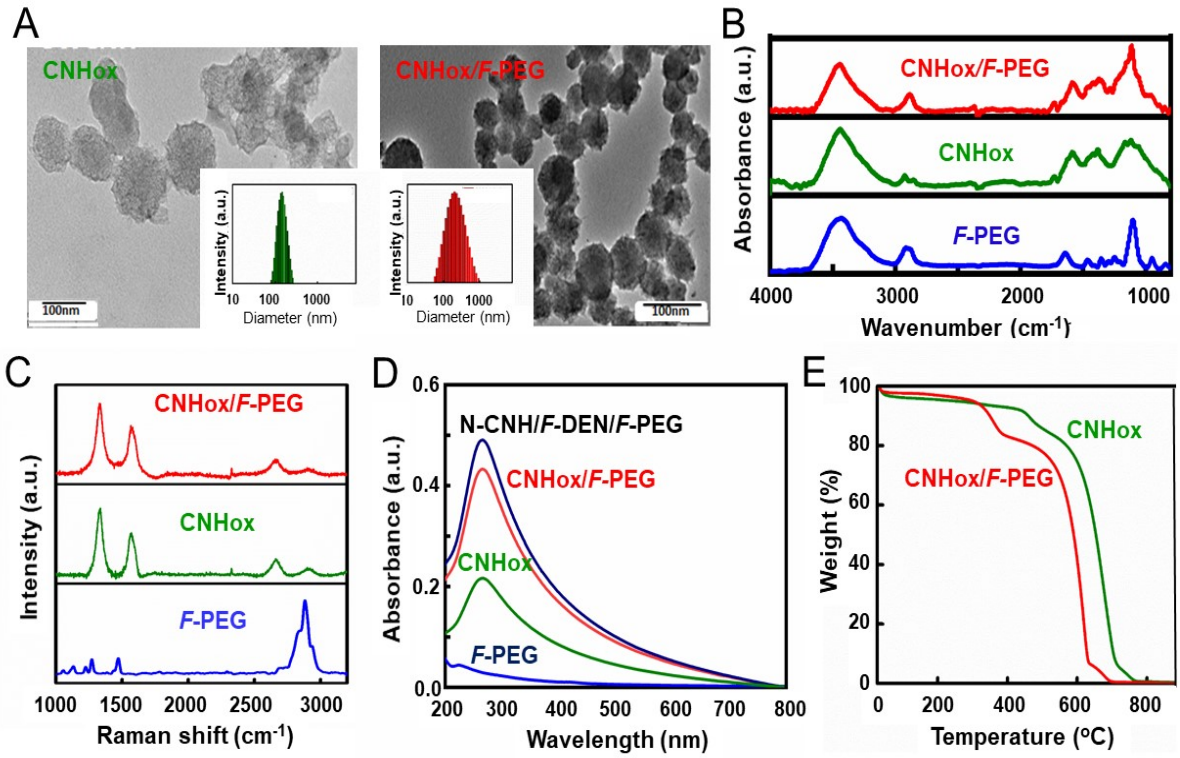

Figure 3 (A) TEM images and DLS results (insets) of CNHox and CNHox/*F*-PEG. (B) FT-IR absorption spectra and (C) Raman spectra of *F*-PEG, CNHox and CNHox/*F*-PEG. (D) UV-visible absorption spectra for aqueous solutions of *F*-PEG (24 mg/l), CNHox (20 mg/l), CNHox/*F*-PEG (CNHox:*F*-PEG weight ratio of 25:24) and N-CNH/*F*-DEN/*F*-PEG (25:24 wight ratio of N-CNH/*F*-DEN:*F*-PEG). (E) TGA of CNHox and CNHox/*F*-PEG.

The Raman spectra of *F*-PEG, CNHox, and CNHox/*F*-PEG are presented in **Figure 3C**. The alkyl chain of *F*-PEG vibrated at 2938, 2883 and 2847 cm^{-1}. The scissoring, wagging and twisting vibration modes of CH_2 bonds appeared at 1470 cm^{-1}, 1271 cm^{-1}, and 1132 cm^{-1}, respectively, and additionally a C-O-C stretching vibration mode was seen at 1057 cm^{-1}. The bands at 1224 and 835 cm^{-1} were assigned to the C-F stretching and carbon skeleton vibration modes of *F*-PEG. On the other hand, CNHox displayed a D band at 1331 cm^{-1}, G band at 1565 cm^{-1},[31] and 2D and 1D bands at 2662 and 2904 cm^{-1}, respectively.[35] Though the corresponding bands of CNHox/*F*-PEG

composite were observed at 1313, 1575, 2666 and 2910 cm^{-1}, the coexistence of *F*-PEG with CNHox was not evidenced from the Raman spectra because Raman bands of *F*-PEG were not detected due to the relatively weak band intensity of *F*-PEG, despite the fact that such confirmation was obtained by FT-IR spectra, as described above.

To study the CNHox/*F*-PEG composite, the UV-visible absorption spectra were measured in water. As presented in **Figure 3D**, a band at 267 nm assigned to the π-π* electronic transition was observed in the spectrum of CNHox. Although the hybridization of *F*-PEG on CNHox did not change this band position, the absorbance was increased due to the improved dispersibility. The absorption spectrum of N-CNH/*F*-DEN/*F*-PEG also slightly showed intensified absorbance without wavelength variation, indicating less influence of *F*-DEN and N-CNH.

The thermal stability of CNHox and CNHox/*F*-PEG was examined by TGA under air flow. As shown in **Figure 3E**, the thermogram of CNHox revealed a loss of 3% in mass below 100 °C assigned to the removal of adsorbed water and other small molecules. The first small (4%) decomposition of CNHox occurred below 420 °C and the additional decomposition of about 9% was observed below 530 °C. The main decomposition appeared below 720°C with a loss of 77% of the total mass. The remaining 7% mass from graphitic impurities was burnt from 720°C to 785°C.[36] CNHox/*F*-PEG showed a similar four-step decomposition process despite the presence of *F*-PEG. The weight loss of CNHox/*F*-PEG was 2% below 100 °C, 16 % below 420 °C, 74% below 630 °C, and 8% below 710 °C. Thus, the presence of *F*-PEG induced a decrease (by about 65°C) of the decomposition temperature.

XRD patterns of *F*-PEG, CNHox and CNHox/*F*-PEG were measured to get the information on the crystalline structure of composites. As presented in **Figure 4A**, *F*-PEG showed the monoclinic crystalline structure (JPCDS No 52–2279) with major peaks at 19.05° (120) and 23.3° ($\bar{1}$31), and minor peaks at 14.69° (021) and 26.18° ($\bar{2}$24).[31] The XRD pattern of CNHox exhibited a main peak at 26.04° and a minor peak at 43.00° indexed at (002) and (100), respectively, for the orthorhombic crystalline structure (JPCDS No 51-2219).[26] However, CNHox/*F*-PEG showed the orthorhombic crystalline structure (JPCDS No 43-1951) with peaks at 25.99° (002) and 44.85° (100), reflecting the crystal structure of CNHox, but the peaks reflecting the *F*-PEG crystal structure were not found because *F*-PEG bound on CNHox gave rise to its crystallographic variation.

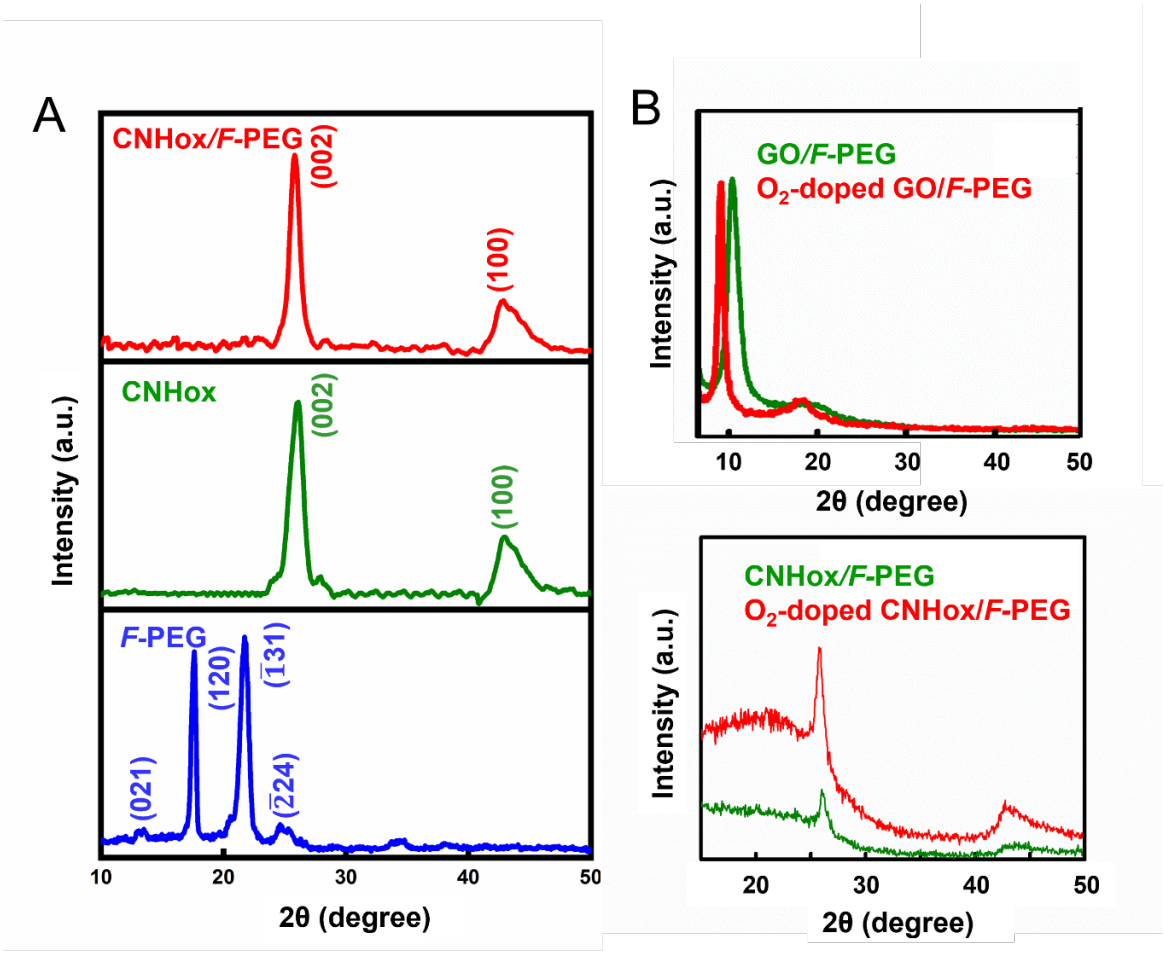

Figure 4 (A) XRD patterns of *F*-PEG, CNHox, and CNHox/*F*-PEG. (B) XRD patterns of GO/*F*-PEG and CNHox/*F*-PEG in the presence or absence of O_2 doping.

O_2 Uptake and Adsorption Kinetics Analysis

The efficiency of materials to load O_2 was measured by exposing them for 8 h to air filled in a closed system. **Figure 5A** presents the O_2 uptake kinetics by the various materials. The O_2 loaded in materials initially increased with the time of exposure to air and then reached the saturation. As presented in **Figure 5A(a)**, the maximum amount of oxygen uptake at 24 h by CNHox, CNHox/*F*-PEG, GO and GO/*F*-PEG was 26.6 ± 2.7, 58.6 ± 4.0, 30.1 ± 2.6, and 54.6 ± 4.2 mg/g, respectively. These results indicate that CNHox and GO uptake a similar amount of O_2 because of their similar graphitic structure. However, when the materials were coated by *F*-PEG, the uptake almost doubled for both graphitic composites because of the presence of the oxygen-adsorbing moiety of fluorinated PEG.

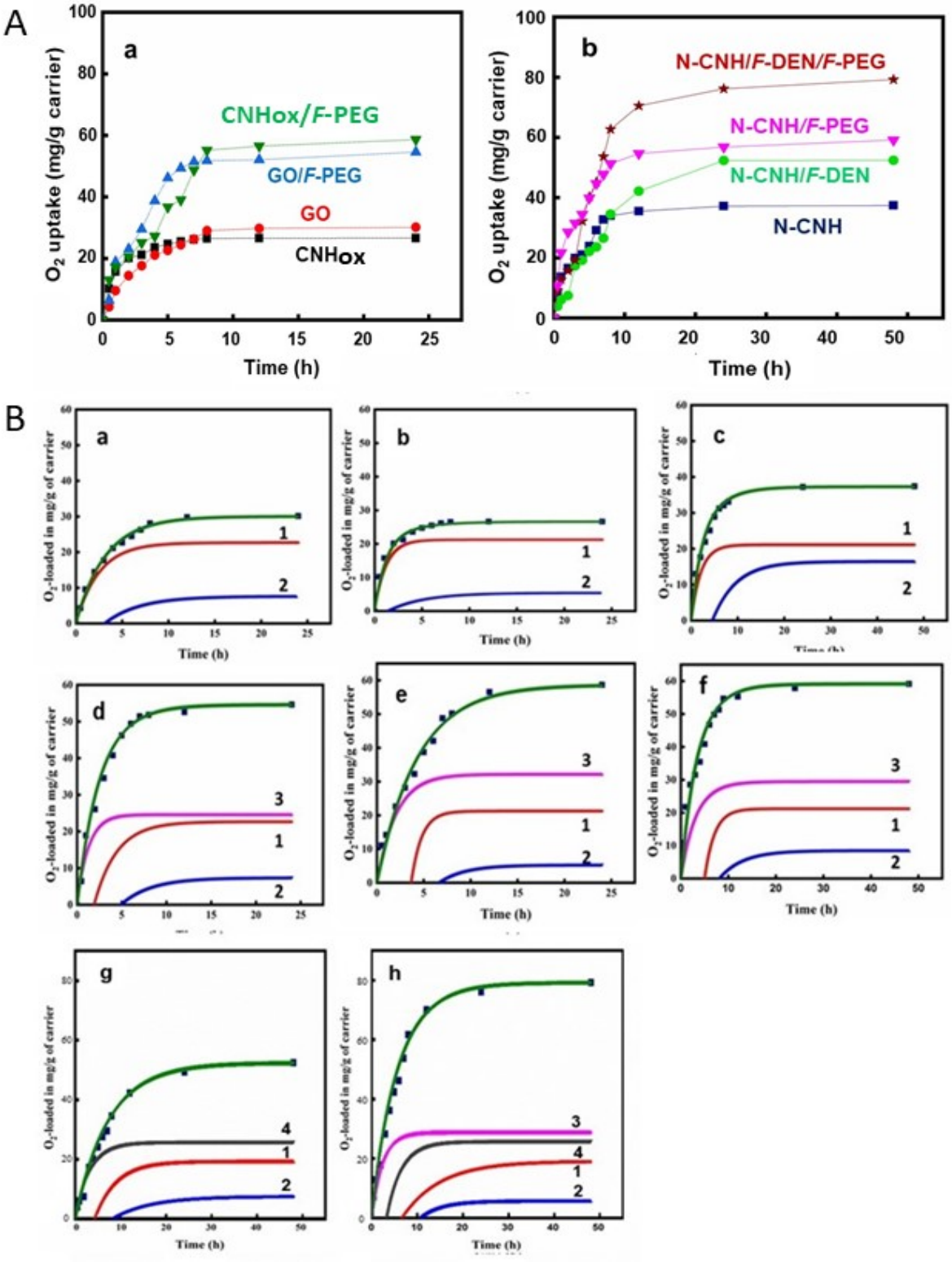

Figure 5 (A) O_2 uptake in (a) GO, GO/*F*-PEG, CNHox, CNHox/*F*-PEG and (b) N-CNH, N-CNH/*F*-PEG, N-CNH/*F*-DEN, and N-CNH/*F*-DEN/*F*-PEG. (B) Computer simulation based on a

multi-site Langmuir adsorption kinetics model for oxygen adsorption on 1, 2, 3, and 4 sites for (a) GO, (b) CNHox, (c) N-CNH, (d) GO/*F*-PEG, (e) CNHox/*F*-PEG, (f) N-CNH/*F*-PEG, (g) N-CNH/*F*-DEN and (h) N-CNH/*F*-DEN/*F*-PEG. Green lines indicate the summation of oxygen adsorption on each site in comparison with the observed data.

In a similar way, the O_2 uptake efficiencies of N-CNH (37.4 ± 2.9 mg/g), N-CNH/*F*-DEN (52.4 ± 4.5 mg/g), N-CNH/*F*-PEG (59.2 ± 7.7 mg/g), and N-CNH/*F*-DEN/*F*-PEG (79.2 ± 5.7 mg/g) were obtained for 48 h, as displayed in **Figure 5A(b)**. The nitrogen doping in CNHox could provide oxygen binding sites and resulted in a higher O_2 uptake efficiency by N-CNH as compared with CNHox. Both N-CNH/*F*-DEN and N-CNH/*F*-PEG composites showed higher O_2 uptakes than N-CNH. N-CNH/*F*-DEN/*F*-PEG revealed the highest O_2 uptake efficiency and was found superior to the other materials. These efficiencies originate from a combination of features: the large cavity of the dendrimers susceptible to encapsulate small molecules,[37,38] specific interaction of oxygen to tertiary amine in PAMAM dendrimers.[39] The interior void space within the PAMAM dendrimer component is important for storing oxygen. It is noteworthy that this interior void space is only available when the dendrimer possesses symmetrical branch cells. In contrast, Denkwalter-type dendrimers derived from asymmetrical branch cells do not exhibit interior void space and hence lack the ability to encapsulate guest molecules.[40] O_2-dissolving property of *F*-PEG[6] and affinity of oxygen to ether groups in PEG. Additionally, the void volume and the interstitial nanospaces constructed in the hierarchical structure consisting of hydrophobic graphitic carbon, hydrophilic dendrimer, oleophobic perfluorocarbons and hydrophilic PEG also increase the O_2 storage efficiency of composites.

The time dependent O_2 uptake profiles in **Figure 5(B)** exhibited a Langmuir monolayer-type adsorption kinetics.[29] Thus, the oxygen adsorption kinetics and mechanism on materials can be interpreted using the principles of Langmuir monolayer adsorption theory.[30] As the materials are constructed by multiple components, the adsorption of oxygen likely happens on multiple adsorption sites. Thus, a single site adsorption model is not pertinent for the present materials, and multiple binding site models must be applied. If multiple adsorption sites are independent, a Langmuir adsorption kinetics equation can be described as a sum of a kinetics equation at each binding site, that is,[29]

$$WO_2 = \Sigma W_i O_2\infty \{1 - \exp(-K_{i\ obs}\ t)\} \qquad (2)$$

where WO_2 is the total adsorbed amount of oxygen at adsorption time t, $W_iO_2\infty$ is the adsorbed amount of oxygen at $t = \infty$ on adsorption site i (= 1 to i), and $K_{i\ obs}$ is the rate constant in the adsorption site i. Assuming the number of adsorption sites on materials, oxygen uptake results presented in **Figure 5B** can be analyzed by a computer simulation based on a Langmuir adsorption monolayer equation for multiple binding sites as described in **Eq 2**.

Th oxygen adsorption kinetics of the various composites were computed, and the results of simulation were compared to the experimental data (**Figure 5B)**. The calculated parameters are listed in **Table 1**. Although GO, CNHox and N-CNH are composed of a single substance, the fitting using a one-site equation was not adequate, and a two-site equation had to be applied. On GO, CNHox and N-CNH, the monolayer formation on the site 1 started together with the beginning of the adsorption process and reached saturation at an earlier time stage (5-10 h). Moreover, $WO\infty$ of site 1 was approximately similar (~20 mg/g) for the three materials. This site is thus expected to be the graphitic structure of the carbon materials, where O_2 adsorbs by van der Waals attraction. The adsorption on site 2 starts about 2-5 h after the beginning of adsorption on site 1, and its $WO\infty$ was increased in the following sequence: CNHox < GO < N-CNH. This result can be explained by the difference of functional binding sites in the graphitic carbons investigated. CNHox has fewer binding sites (only C=O) but GO was acid-treated and thus possesses functional carboxylic acid, ether, and hydroxyl groups besides ketone. Since nitrogen-containing moieties were introduced in N-CNH after acid-treatment, N-CNH has more active attraction sites for oxygen than GO.

The O_2 uptake profiles of GO/*F*-PEG, CNHox/*F*-PEG and N-CNH/*F*-PEG composites were best fitted using a three-site equation. The adsorption profiles of oxygen at sites 1 and 2 were almost similar to those of GO, CNHox and N-CNH, although their kinetics started after 2-5 h and 5-8 h, respectively. Since the adsorption on site 3 started soon after the beginning of the adsorption process, this site should be located on *F*-PEG. The oxygen uptake on site 3 was superior to those on sites 1 and 2 because of the location of *F*-PEG in the composite outer shell where O_2 molecules are first adsorbed. The delay in the start time of adsorption on sites 1 and 2 might be due to the diffusion time of O_2 to the graphitic carbon through the *F*-PEG shell layer. Since *F*-PEG coats the external surfaces of GO, CNHox and N-CNH, a fast adsorption may occur on *F*-PEG and the slow diffusion of O_2 should arise with time toward the graphitic carbon cores with sites 1 and 2. The fitting curve for N-CNH/*F*-DEN indicates that the O_2 adsorption occurred at two sites on N-CNH

and one site on *F*-DEN. The behavior in **Figure5B(g)** resembles to cases illustrated in Figure **5B(d, e & f)**. That is, *F*-DEN, which forms an outer shell, provides a site onto which oxygen is rapidly adsorbed. A similar trend was confirmed for N-CNH/*F*-DEN/*F*-PEG. The fitting curves of N-CNH/*F*-DEN/*F*-PEG indicated four sites, which can be assigned to *F*-PEG, *F*-DEN, the graphitic structure, and the functional groups on the graphitic structures. O_2 adsorbed first on *F*-PEG and successively diffused to the other sites.

Table 1. Parameters obtained from computer simulation for O_2 uptake curves using a multi-site Langmuir adsorption kinetics equation.

Binding site	site 1		site 2		site 3		site 4		
Carrier	$W_1O_{2\infty}$ (mg/g)	K_{1obs} (h^{-1})	$W_2O_{2\infty}$ (mg/g)	K_{2obs} (h^{-1})	$W_3O_{2\infty}$ (mg/g)	K_{3obs} (h^{-1})	$W_4O_{2\infty}$ (mg/g)	K_{4obs} (h^{-1})	r^2
GO	22.66	0.401	7.49	0.298					0.996
CNHox	21.11	0.900	5.40	0.367					0.998
N-CNH	21.11	0.483	16.31	0.201					0.998
GO/*F*-PEG	22.66	0.401	7.49	0.298	24.47	0.782			0.996
CNHox/*F*-PEG	21.11	0.900	5.40	0.367	32.02	0.501			0.997
N-CNH/*F*-PEG	21.11	0.483	8.34	0.201	29.61	0.309			0.995
N-CNH/*F*-DEN	19.06	0.213	7.49	0.121			25.89	0.303	0.997
N-CNH/*F*-DEN/*F*-PEG	19.06	0.213	5.49	0.121	28.77	0.417	25.89	0.303	0.996

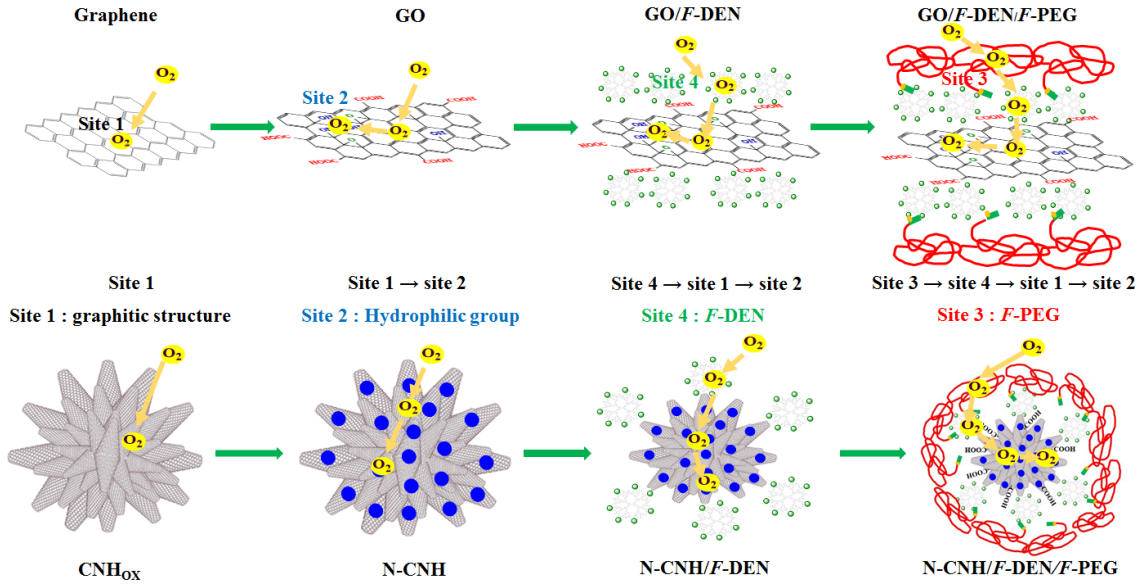

Figure 6 Schematic illustration of O_2 adsorption on GO/*F*-DEN/*F*-PEG and N-CNH/*F*-DEN/*F*-PEG.

From the above analysis, four binding sites of O_2 adsorption were identified in the materials. Although the O_2 adsorption on functional groups was low (5.4-8.3 mg/g), except for N-CNH, the other sites (graphitic carbons, *F*-PEG, and *F*-DEN) displayed comparably high oxygen uptake capacity (19-32 mg/g), although their kinetic constants were dependent on both materials and sites. Thus, O_2 adsorbed almost evenly on functional graphitic carbon, *F*-PEG and *F*-DEN in composites and the kinetic constants were also reasonable. The peculiarity of composites in this study is the multistep adsorption of oxygen: the oxygen first being adsorbed in the outer shell and penetrated into the inner shell or interior core after a delay of 10-30 h. **Figure 6** illustrates adsorption sites and adsorption processes of O_2 in materials. This behavior may be ascribable to the hierarchical structure of nanocomposites.

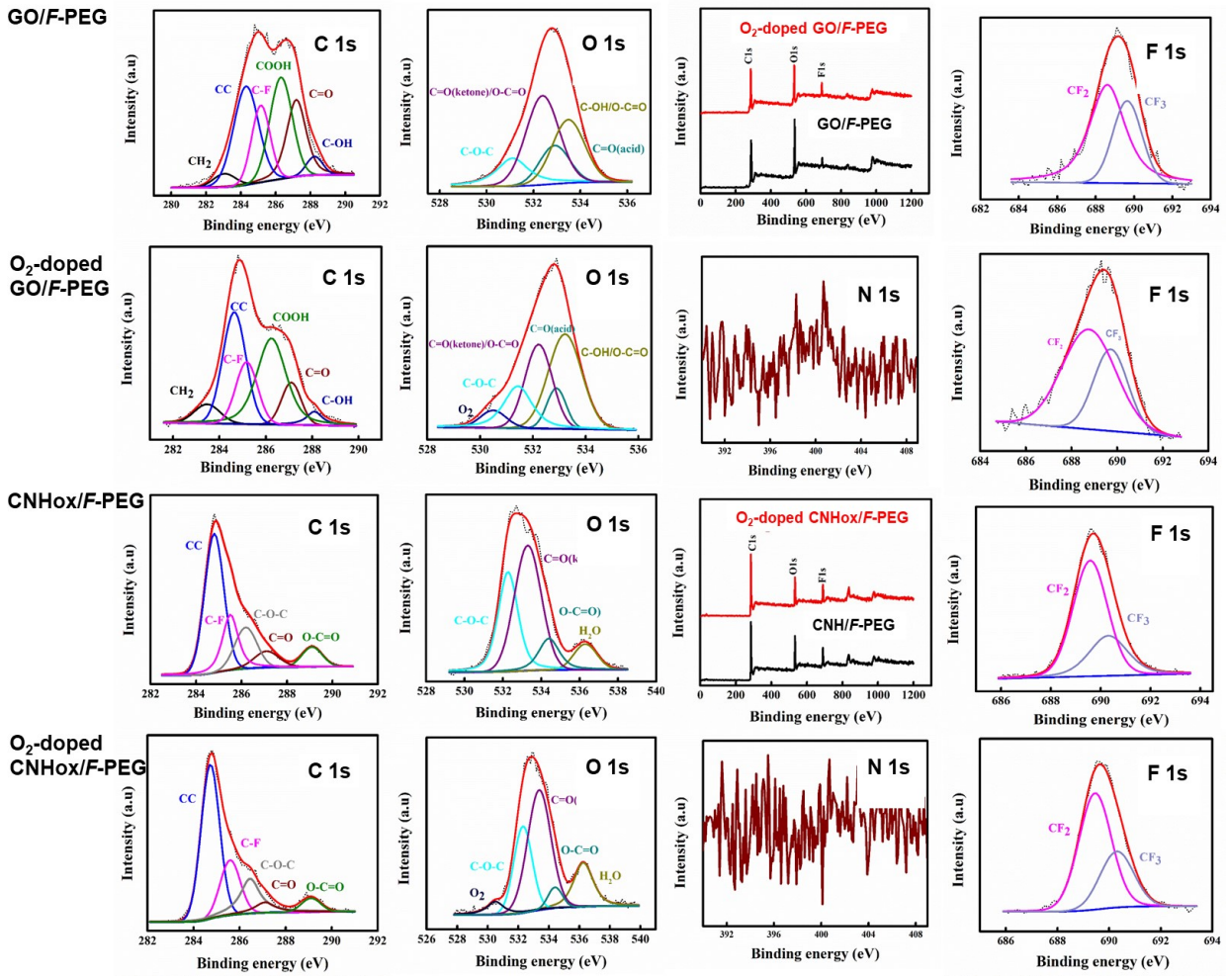

Figure 7 XPS survey spectra of GO/*F*-PEG, O_2-doped GO/*F*-PEG, CNHox/*F*-PEG and O_2-doped CNHox/*F*-PEG and their elemental deconvolution spectra of C 1s, O1s, N 1s and F 1s.

The XPS of GO/*F*-PEG and CNHox/*F*-PEG was investigated before and after O_2 loading to study the effects on chemical composition. The survey scans, fine analyses and deconvolution peaks are shown in **Figure 7**. The survey scan displayed peaks of C 1s, N 1s, O 1s, and F 1s, which came from *F*-PEG, GO or CNHox. GO/*F*-PEG showed deconvoluted C 1s species of aromatic (CC), carboxylic acid (COOH), ketone (C=O), phenol (C-OH), alkyl (CH_2) and carbon-fluorine (C-F) species attributed to GO and *F*-PEG. O 1s fine analysis showed chemical species of ketone (C=O), carboxylic acid (C=O and OH) and phenol (OH) from GO and ether (COC) from *F*-PEG. The C=O and C-O bonds of ester showed similar binding energies. The composite GO/*F*-PEG also showed additional F 1s peaks originated from the fluorinated moiety (CF_2 and CF_3) of *F*-PEG.[31]

C 1s of CNHox/*F*-PEG exhibited aromatic (CC), ketone (C=O), alkyl (CH_2), and carbon-fluorine (C-F), which were ascribed to *F*-PEG and CNHox. O 1s fine analysis displayed chemical species of ketone (C=O) from CNHox, and ether (COC) and ester (C=O and C-O) from *F*-PEG. The F 1s peaks originated from CF_2 and CF_3 of *F*-PEG. As shown in **Table S1**, the binding energies and area intensities of deconvoluted peaks from GO/*F*-PEG and CNHox/*F*-PEG did not change after O_2-loading, indicating that there is no influence on the chemical natures of the composites. However, it was clearly displayed that both GO/*F*-PEG and CNHox/*F*-PEG showed molecular oxygen (O_2) at 530.5 eV after O_2 loading. The existence of these new peaks in O_2-loaded composites confirms the uptake of oxygen as O_2 molecules in composites.[41-43] Although air was used in this study, N 1s was negligible in the O_2-doped composites. These results indicate that N_2 gas was not trapped in composites.

To study the effects of O_2 adsorption on the crystalline structure of composites, XRD measurements were conducted. The XRD patterns of GO/*F*-PEG and CNHox/*F*-PEG before and after O_2 uptake are presented in **Figure 4B**. The (001) diffraction peak of GO/*F*-PEG shifted from its original position 10.69° to 9.29° after the O_2 uptake. This variation indicates an increase of the graphene sheet interdistance from 0.83 nm to 0.95 nm. The adsorption of O_2 in GO/*F*-PEG composite caused the interlayer expansion of graphene sheets due to the adsorption-induced deformation effect. In the same way, the major (002) and minor (100) peaks of CNHox/*F*-PEG changed from 25.99° to 25.74° and from 44.85° to 42.57°. However, since these angle changes corresponded to distance variations from 0.34 nm to 0.35 nm and from 0.20 nm to 0.21nm, respectively, indicating that the the crystallographic modification of CNHox is negligibly small.

The distance between graphene sheets in GO/*F*-PEG was expanded by 0.12 nm due to the intercalation of O_2. This variation is comparable to the 0.31 nm expansion of the interlayer distance of GO caused by the NO uptake.[31] However, since the orthorhombic crystallographic structure of CNHox in CNHox/*F*-PEG was not changed, oxygen should be adsorbed on the single wall surface or in the interior of the CNHox structure and additionally in a *F*-PEG domain of the CNHox/*F*-PEG composite. It was clearly shown that the self-assembled structure of GO/*F*-PEG was expanded due to the adsorption-induced deformation effect of O_2, but CNHox/*F*-PEG was not affected due to the single-walled structure of CNHox.

O_2 release and singlet oxygen generation studies

For O_2 to be useful in the cellular function, its release from composites must be well-controlled and slow. After saturation of carriers with O_2, the amount of oxygen released was determined by TGA at 37 °C. As seen in **Figure 8**, an initial decrease of weight loss happened within 20 min for GO and GO/*F*-PEG and within 10 min for CNHox and CNHox/*F*-PEG. For all carriers, however, the high amount (> 90%) of oxygen remained without release. After this initial weight loss, no additional weight loss was observed until 400 min. However, the O_2 release from carriers decreased in the order of GO > GO/*F*-PEG > CNHox > CNHox/*F*-PEG, although the O_2 uptake was CNHox < GO << GO/*F*-PEG < CNHox/*F*-PEG. Thus, the O_2 release was faster from GO than for CNHox and for the composites coated with *F*-PEG. These trends can depend on the number of binding sites and the interaction of oxygen with these binding sites.

Singlet oxygen radical $^1O_2$ generates by the nanocomposites after LED irradiation. Then, a triplet-state photosensitizer ($^3T_1$), which was excited by light adsorption, transfers energy to a ground state oxygen ($^3O_2$). A singlet oxygen ($^1O_2$) is thus generated, and an energy-lost photosensitizer comes down a ground-state ($^1S_0$). Thus, singlet oxygen generation was evaluated using an anthracene probe.[32,44] As shown in **Table 2**, the $^1O_2$ generation was the lowest for GO. Acid-treated CNH generated more $^1O_2$ than CNHox, and the production was further increased after N-loading. The addition of *F*-DEN on GO and N-CNH increased the $^1O_2$ generation, and further addition of *F*-PEG further increased it. Moreover, the tendency for $^1O_2$ production is in proportion to the O_2 uptake in carriers except for GO (**Figure 5A**). The $^1O_2$ production capabilities have been reported for different generators using different detection techniques, such as UV-visible absorption spectroscopy,[45] fluorescence,[28,32,46-48] and electron paramagnetic resonance.[49]

Moreover, its quantitative evaluation depended on the evaluation technology. Then singlet oxygen production was mainly expressed using singlet oxygen quantum yields[28,46-48] or using singlet oxygen generation values[28,32] obtained from fluorescence data. The latter values calculated using equation (1) increased in the order of Au nanoparticle (AuNP) < Fe_3O_4NP@carbon dot (Cdot) < AuNP/Fe_3O_4NP@Cdot < porphyrin derivative (TCPP) < AuNP/TCPP < AuNP/Fe_3O_4NP@Cdot/TCPP and with their concentration. Thus, the highest value (20 mmol/g(material)) was obtained for AuNP/Fe_3O_4NP@Cdot/TCPP at 10 μg/ml concentration.[28] This value was smaller than the current CNH-based generators. It is noteworthy that this value is smaller than those reported for the CNH-based nanocomposites of the present work. These results indicate that the O_2-loaded nanocomposites and, particularly, the composites containing fluorinated moieties could be used for photodynamic therapy, in which the efficiency depends on the amount of O_2 loaded.

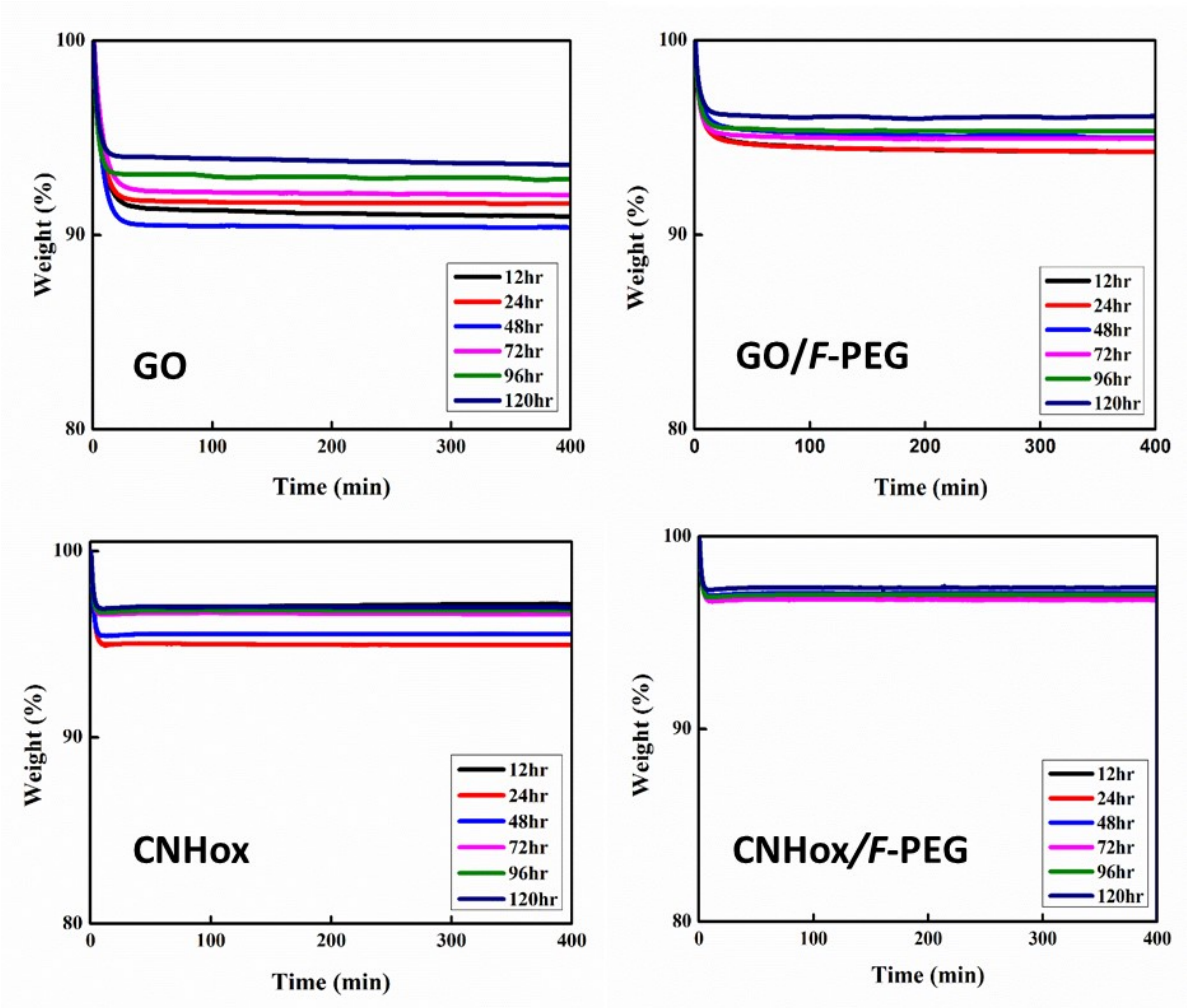

Figure 8. O_2 release profiles from O_2-loaded GO, GO/*F*-PEG, CNHox, and CNHox/*F*-PEG after O_2 loading at different durations.

Table 2 Singlet oxygen generation and oxygen uptake for the various nanocomposites.

Material	Generated $^1O_2$ (mmol/g(material))	oxygen uptake at 24 h (mg/g(material))
GO	8.9 ± 0.3	30.1±2.6
N-GO/*F*-DEN	16.4 ± 2.5	
CNHox	14.3 ± 3.5	
CNH	20.0 ± 2.3	26.6±2.7
N-CNH	25.4 ± 1.1	37.4±2.9
N-CNH/*F*-DEN	27.8 ± 2.3	52.4±4.5
N-CNH/*F*-DEN/*F*-PEG	44.9 ± 0.3	79.2±5.7

CONCLUSIONS

Various graphene oxide- or carbon nanohorn-based nanomaterials (GO, CNH, CNHOx, N-CNH) and assembled nanocomposites that also comprise dendrimers and pegylated perfluoroalkylated components (GO/*F*-PEG, CNH/*F*-PEG, N-CNH/*F*-PEG, N-CNH/*F*-DEN, and N-CNH/*F*-DEN/*F*-PEG) were prepared and investigated as potential O_2 reservoir materials. It is important to note that all the various components of the hierarchical structures are linked by chemical bonding, except *F*-PEG, which is physically adsorbed on the nanomaterials. In addition to the van der Waals attraction to O_2 developed by graphitic materials, the hydrophilic functional groups present at their surface is expected to interact electrostatically and through hydrogen bonding with oxygen. The PAMAM dendrimer has enough void volume to encapsulate small molecules[37] and *F*-PEG derivatives have proven significant O_2 carrying capacity.[50] Especially, perfluorocarbon domains formed by *F*-DEN and *F*-PEG offer hydro- and oleo-phobic domains that are prone to accommodate O_2. Thus, the hierarchical structures considered here that consist of differently functionalized components could offer a high O_2 storage efficiency. It was shown that the O_2 uptake efficiency strongly depended on materials. It increased for acid-treating and N-doping in the CNHox nanomaterial, due to the resultant increase in functional group number, which provide oxygen- and nitrogen-based binding sites for O_2. These materials show similar adsorption profiles reflecting O_2 adsorption on binding sites. The O_2 uptake efficiency was further enhanced in the *F*-PEG and/or *F*-DEN-grafted nanocomposites GO/*F*-PEG, CNHox/*F*-PEG, N-CNH/*F*-PEG, and N-CNH/*F*-DEN. The ternary composite N-CNH/*F*-DEN/*F*-PEG that combines

two fluorinated moieties provided the ultimate in terms of O_2 loading. Three steps were identified by the adsorption kinetics analysis when *F*-PEG or *F*-DEN domains are present. O_2 adsorbs first on the outer shell, then additional O_2 penetrates the inner shell and finally reaches the carbonaceous core in a nanocomposite. It is likely that the hydro- and oleophobic interactions developed by the perfluorinated chains in *F*-DEN and *F*-PEG create domains particularly prone to solubilize O_2. One characteristic of the present composites is their hierarchical structures, in which each component species additively contributes to improve the O_2 adsorption capacity. All O_2 release profiles show an initial rapid but limited release, while most of the O_2 remains entrapped for long periods of time (at least 400 min). The presence of the perfluorinated moieties prolongs the release of O_2, which is advantageous when sustained delivery is required. The O_2 uptake/release behavior of the present composites differs markedly from the case of nitric oxide gas from related composites.[26,31] Although the uptake of O_2 in the composites was lower than that of NO, the amount of O_2 release is limited to 10% maximum, while the amount of NO is faster and total due to the propensity to oxidization in NO_2. Similarly, N_2 coexisting in air may not be reserved because of no specific binding site for this inert gas in nanocomposites. On the other hands, CO_2 gas on nitrogen-based binding sites may inhibit the O_2 adsorption since CO_2 easy binds on nitrogen-based binding sites in carbon material and dendrimer.[30] Finally, it was shown that the nanocomposites can serve as oxygen reservoirs from which singlet $^1O_2$ can be produced under LED irradiation. Altogether, this study suggests that such nanocomposites could be used for tissue oxygenation and singlet oxygen generation, which has potential in oxygen-dependent cancer therapies.

ASSOCIATED CONTENT

Supporting Information

The Supporting Information is available free of charge at https://pubs.acs.org/doi/

It includes one Table and two Figures. Table S1 displays the binding energy and area intensity from XPS spectra of the nanocomposites before and after O_2 loading. Figure S1 provides a scheme illustrating the synthesis of GO/*F*-DEN, a photograph of an aqueous dispersion of GO/*F*-DEN, the IR absorption spectra of GO, pentafluoropropionic acid (PFPrA), DEN(OH), GO/DEN(OH) and GO/*F*-DEN, and an EDS analysis of GO/*F*-DEN carried out on an electron micrograph. Figure S2

provides the hydrodynamic particle sizes, zeta potentials for some of the composites, including GO/*F*-DEN/*F*-PEG and schematic models of adsorption of *F*-PEG on GO and GO/*F*-DEN.

AUTHOR INFORMATION

Corresponding Authors

Toyoko Imae - Graduate Institute of Applied Science and Technology, National Taiwan University of Science and Technology, Taipei 10607, Taiwan; orcid.org/0000-0003-2731-1960; Email: imae@mail.ntust.edu.tw (T.I.)

Marie Pierre Krafft - University of Strasbourg, Charles Sadron Institute (CNRS), France; orcid.org/0000-0002-3379-2783: Email:krafft@unistra.fr (M.P.K.)

Notes

The authors declare no competing financial interest.

ACKNOWLEDGEMENTS

This research was partially supported by a grant from the France/Taiwan Program of Integrated Actions (PIA) Orchid (MPK travel grant to Taipei). YAW, JHR and NK were financially supported by National Taiwan University of Science and Technology, Taiwan, for student scholarships. The authors would like to acknowledge Dr. C.-C. Chang for her research assistance.

REFERENCES

1. Vaupel, P.; Mayer, A.; Höckel, M., Tumor Hypoxia and Malignant Progression. *Method Enzymol.* **2004,** *381*, 335-354.
2. Nakazawa, M. S.; Keith, B.; Simon, M. C., Oxygen Availability and Metabolic Adaptations. *Nat. Rev. Cancer* **2016,** *23*, 663–673.
3. Gilkes, D. M.; Semenza, G. L.; Wirtz, D., Hypoxia and the Extracellular Matrix: Drivers of Tumour Metastasis. *Nat. Rev. Cancer* **2014,** *14*, 430-439.
4. Riess, J. G., Highly Fluorinated Systems for Oxygen Transport, Diagnosis and Drug Delivery. *Colloids Surf. A: Physicochem. Eng. Aspects* **1994,** *84*, 33-48.

5. Riess, J. G.; Krafft, M. P., Fluorinated Materials for in *Vivo* Oxygen Transport (Blood Substitutes), diagnosis and drug delivery. *Biomaterials* **1998,** *19*, 1529-1539.
6. Riess, J. G., Injectable Oxygen Carriers (Blood Substitutes) - Raison D'être, Chemistry, and some Physiology. *Chem. Rev.* **2001,** *101* (9), 2797-2920.
7. Winslow, R. M., *Blood Substitutes*. Elsevier: Amsterdam, 2006.
8. Modery-Pawlowski, C. L.; Tian, L. L.; Pan, V.; Sen Gupta, A., Synthetic Approaches to RBC Mimicry and Oxygen Carrier Systems. *Biomacromolecules* **2013,** *14*, 939-48.
9. Feng, L.; Betzer, O.; Tao, D.; Sadan, T.; Popovtzer, R.; Liu, Z., Oxygen Nanoshuttles for Tumor Oxygenation and Enhanced Cancer Treatment. *CCS Chem.* **2019,** *1*, 239–250.
10. Krafft, M. P., Alleviating Tumor Hypoxia with Perfluorocarbon-Based Oxygen Carriers. *Curr. Opin. Pharmacol.* **2020,** *53*, 117-125.
11. Sahu, A.; Kwon, I.; Tae, G., Improving Cancer Therapy Through the Nanomaterials-Asisted Alleviation of hypoxia. *Biomaterials* **2020,** *228*, 119578.
12. Krafft, M. P.; Riess, J. G., Therapeutic Oxygen Delivery by Perfluorocarbon-Based Colloids. *Adv. Colloid Interface Sci.* **2021,** *294*, 102407.
13. Yao, Y.; Zhang, M.; Liu, T.; Zhou, J.; Gao, Y.; Wen, Z.; Guan, J.; Zhu, J.; Lin, Z.; He, D., Perfluorocarbon-Encapsulated PLGA-PEG Emulsions as Enhancement Agents for Highly Efficient Reoxygenation to Cell and Organism. *ACS Appl. Mater. Interfaces* **2015,** *7*, 18369-78.
14. Krafft, M. P.; Riess, J. G., Perfluorocarbons, Life Sciences and Biomedical Uses. *J. Polymer Sci. Part A: Polymer Chem.* **2007,** *45*, 1185-1198.
15. Maio, A.; Scaffaro, R.; Lentini, L.; Palumbo Piccionello, A.; Pibiri, I., Perfluorocarbons–Graphene Oxide Nanoplatforms as Biocompatible Oxygen Reservoirs. *Chem. Eng. J.* **2018,** *334*, 54-65.
16. Komaty, S.; Anfray, C.; Zaarour, M.; Awala, H.; Ruaux, V.; Valable, S.; Mintova, S., A Facile Route Toward the Increase of Oxygen Content in Nanosized Zeolite by Insertion of Cerium and Fluorinated Compounds. *Molecules* **2018,** *23*, 37-49.
17. Georgakilas, V.; Tiwari, J. N.; Kemp, K. C.; Perman, J. A.; Bourlinos, A. B.; Kim, K. S.; Zboril, R., Noncovalent Functionalization of Graphene and Graphene Oxide for Energy Materials, Biosensing, Catalytic, and Biomedical Applications. *Chem. Rev.* **2016,** *116*, 5464-519.

18. Ajima, K.; Yudasaka, M.; Murakami, T.; Maigné, A.; Shiba, K.; Iijima, S., Carbon Nanohorns as Anticancer Drug Carriers *Mol. Pharm.* **2005,** *2*, 475-480.
19. Liu, X.; Li, H.; Wang, F.; Zhu, S.; Wang,Y.; Xu, G., Functionalized Single-Walled Carbon Nanohorns for Electrochemical Biosensing. *Biosens Bioelectron.* **2010**, *25*, 2194–2199.
20. Shen, F.; Zhang, C.; Cai, Z.; Wang, J.; Zhang, X.; Machuki, J.O.; Shi, H.; Gao, F., Carbon Nanohorns/Pt Nanoparticles/DNA Nanoplatform for Intracellular Zn^{2+} Imaging and Enhanced Cooperative Phototherapy of Cancer Cells. *Anal. Chem.* **2020,** *92*, 16158-16169.
21. Siriviriyanun, A.; Tsai, Y. J.; Voon, S. H.; Kiew, S. F.; Imae, T.; Kiew, L. V.; Looi, C. Y.; Wong, W. F.; Lee, H. B.; Chung, L. Y., Cyclodextrin- and Dendrimer-Conjugated Graphene Oxide as a Nanocarrier for the Delivery of Selected Chemotherapeutic and Photosensitizing Agents. *Mater. Sci. Eng. C Mater. Biol. Appl.* **2018,** *89*, 307-315.
22. Ma, X.; Shu, C.; Guo, J.; Pang, L.; Su, L.; Fu, D.; Zhong, W., Targeted Cancer Therapy Based on Single-Wall Carbon Nanohorns with Doxorubicin in *Vitro* and in *Vivo*. *J Nanopart Res*, **2014**, *16*, 2497-2511.
23. Lanceta, A.M.; Bosch, M.M.; Lesmes, P.M., Single-Walled Carbon Nanohorns as Promising Nanotube-Derived Delivery Systems to Treat Cancer. *Pharmaceutics*, **2020**, *12*, 850-871.
24. Zhu, S.; Xu, G., Single-Walled Carbon Nanohorns and Their Applications. *Nanoscale*, 2010, *2*, 2538-2549.
25. Gatica, S. M.; Nekhai, A.; Scrivener, A., Adsorption and Gas Separation of Molecules by Carbon Nanohorns. *Molecules* **2016,** *21*, 662-673.
26. Krathumkhet, N.; Sabrina; Imae, T.; Krafft, M. P., Nitric Oxide Gas in Carbon Nanohorn/Fluorinated Dendrimer/Fluorinated Poly(Ethylene Glycol)-Based Hierarchical Nanocomposites as Therapeutic Nanocarriers. *ACS Appl. Bio Mater.* **2021,** *4*, 2591-2600.
27. Kiew, S. F.; Ho, Y. T.; Kiew, L. V.; Kah, J. C. Y.; Lee, H. B.; Imae, T.; Chung, L. Y., Preparation and Characterization of an Amylase-Triggered Dextrin-Linked Graphene Oxide Anticancer Drug Nanocarrier and its Vascular Permeability. *Int. J. Pharm.* **2017,** *534*, 297−307.
28. Do, T. T. A.; Imae, T., Photodynamic and Photothermal Effects of Carbon Dot-Coated Magnetite and Porphyrin-Conjugated Confeito-Like Gold Nanoparticles. *Bull. Chem. Soc. Jpn.* **2021,** *8*, 2079-2088.

29. Shah, K. J.; Imae, T., Selective Gas Capture Ability of Gas-Adsorbent-Incorporated Cellulose Nanofiber Films. *Biomacromolecules* **2016,** *17*, 1653−1661.
30. Shah, K. J.; Imae, T.; Ujihara, M.; Huang, S.-J.; Wu, P.-H.; Liu, S.-B., Poly(Amido Amine) Dendrimer-Incorporated Organoclays as Efficient Adsorbents for Capture of NH_3 and CO_2. *Chem. Eng. J.* **2017,** *312*, 118-125.
31. Workie, Y. A.; Sabrina; Imae, T.; Krafft, M. P., Nitric Oxide Gas Delivery by Fluorinated Poly(Ethylene Glycol)@Graphene Oxide Carrier Toward Pharmacotherapeutics. *ACS Biomater. Sci. Eng.* **2019,** *5*, 2926-2934.
32. Do, T. T. A.; Grijalvo, S.; Imae, T.; Garcia-Celma, M.; Rodríguez-Abreu, C. A Nanocellulose-Based Platform Towards Targeted Chemo-Photodynamic/Photothermal Cancer Therapy, *Carbohydrate Polym.*, 270, **2021**, 118366.
33. Ujihara, M.; Ahmed, M. M. M.; Imae, T.; Yamauchi, Y., Massive-Exfoliation of Magnetic Graphene from Acceptor-Type GIC by Long-Chain Alkyl Amine. *J. Mater. Chem. A* **2014,** *2*, 4244 - 4250.
34. Mitamura, K.; Imae, T., Structure Determination of Hybrid Films of Clay and Clay Dendrimer Nanocomposite on Langmuir-Blodgett Film by X-ray Reflectometry. *Trans. Mater. Res. Soc. Jpn.* **2003,** *28*, 71-74.
35. Lodermeyer, F.; Costa, R. D.; Guldi, D. M., Implementation of Single-Walled Carbon Nanohorns into Solar Cell Schemes. *Adv. Energy Mater.* **2017,** *7*, 1601883-902.
36. Li, N.; Wang, Z.; Zhao, K.; Shi, Z.; Gu, Z.; Xu, S., Synthesis of Single-Wall Carbon Nanohorns by Arc-Discharge in Air and Their Formation Mechanism. *Carbon* **2010,** *48*, 1580-85.
37. Imae, T.; Funayama, K.; Aoi, K.; Tsutsumiuchi, K.; Okada, M.; Furusaka, M., Small-Angle Neutron Scattering and Surface Force Investigations of Poly(Amido Amine) Dendrimer with Hydroxyl End Groups. *Langmuir* **1999,** *15*, 4076-4084.
38. Chu, C.-C.; Imae, T., Fluorescence Investigations of Oxygen-Doped Simple Amine in Comparison with Fluorescent PAMAM Dendrimer. *Macromol. Rapid Commun.* **2009,** *30*, 89-93.
39. Saravanan, G.; Imae, T., Visual Observation and Characterization of Fluorescent Poly(Amido Amine) Dendrimer in Film State. *J. Nanosci. Nanotechnol.* **2011,** *11*, 4838–4845

40. Tomalia, D. A.; Nixon, L.S; Hedstrand, D. M, The Role of Branch Cell Symmetry and Other Critical Nanoscale Design Parameters in the Determination of Dendrimer Encapsulation Properties. *Biomolecules*. **2020**, *10*, 642.
41. Hoenigman, J. R., An XPS Study of the Adsorption of Oxygen and Water Vapor on Clean Lithium Films. *Appl. Surf. Sci.* **1984,** *18*, 207-222.
42. Peuckert, M., On the Adsorption of Oxygen and Potassium Hydroxide on Silver. *Surf. Sci.* **1984,** *146*, 329-340.
43. Jones, T. E.; Rocha, T. C. R.; Knop-Gericke, A.; Stampfl, C.; Schlögl, R.; Piccinin, S., Insights into the Electronic Structure of the Oxygen Species Active in Alkene Epoxidation on Silver. *ACS Catal.* **2015,** *5*, 5846-50.
44. Uchiyama, M.; Momotake, A.; Ikeue, T.; Yamamoto, Y., Photogeneration of Reactive Oxygen Species from Water-Soluble Phthalocyanine Derivatives Bound to a G-Quadruplex DNA. *Bull. Chem. Soc. Jpn*. **2020**, *93*, 1504–1508
45. Siriviriyanun, A.; Imae, T.; Calderó, G.; Solans, C. Phototherapeutic Functionality of Biocompatible Graphene Oxide/Dendrimer Hybrids. *Colloids Surfaces B: Biointerfaces* **2014**, *121*, 469–473.
46. Su C.-H.; Soendoro, A.; Okayama, S., Rahmania, F. J.; Nagai, T.; Imae, T.; Tsutsumiuchi, K.; Kawai N. Drug Release Stimulated by Magnet and Light on Magnetite- and Carbon Dot-Loaded Carbon Nanohorn, *Bull. Chem. Soc. Jpn.* **2022**, *95*, 582-594.
47. Haimov, E.; Weitman, H.; Polani, S.; Schori, H.; Zitoun, D.; Shef, O. Meso-Tetrahydroxyphenylchlorin-Conjugated Gold Nanoparticles as a Tool to Improve Photodynamic Therapy, *ACS Appl. Mater. Interfaces* **2018**, *10*, 2319–2327.
48. Zheng, X. T.; Lai, Y. C.; Tan, Y. N. Nucleotide-derived Theranostic Nanodots with Intrinsic Fluorescence and Singlet Oxygen Generation for Bioimaging and Photodynamic Therapy. *Nanoscale Adv*., **2019**, *1*, 2250–2257.
49. Wu, S.; Zhou, R.; Chen, H.; Zhang, J.; Wu, P. Highly Efficient Oxygen of Carbon Dots: the Role of Nitrogen Doping. *Nanoscale*, **2020**, *2*, 5543-5553.
50. Fan, M.; Alghassab, T. S.; Twyman, L. J., Increased Oxygen Solubility in Aqueous Media using PEG–Poly-2,2,2-Trifluoroethyl Methacrylate Copolymer Micelles and Their Potential Application as Volume Expanders and as an Artificial Blood Product. *ACS Appl. Bio Mater.* **2018,** *1*, 708-713.

Graphical Abstract

GO/*F*-DEN/*F*-PEG

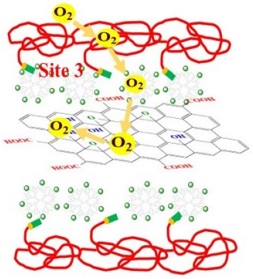

Site 3 : *F*-PEG
Site 4 : *F*-DEN
Site 2 : hydrophilic group
Site 1 : graphitic structure
Site 2 : hydrophilic group
Site 4 : *F*-DEN
Site 3 : *F-PEG*

N-CNH/*F*-DEN/*F*-PEG